PIER C

(Received 12 April 2024, Accepted 6 June 2024, Scheduled 20 June 2024)

Bandwidth and Gain Improvement of Low-Profile MIMO Printed Arrays by Utilizing AMC Surface for Wireless Communications

Hossein Malekpoor*

Department of Electrical Engineering, Faculty of Engineering, Arak University, Arak 38156-8-8349, Iran

ABSTRACT: A compact dual-element microstrip antenna, employing a parasitic artificial magnetic conductor (AMC), is proposed for facilitating 4G and 5G wireless communications. The antenna design entails microstrip dipoles fed by a T-shaped feedline. Notably, the antenna achieves a measured bandwidth of 5.35–6.7 GHz (with $S_{11} \leq -10$ dB). To enhance performance, a proposed parasitic AMC reflector is integrated into the antenna structure. Incorporating a 3×3 AMC array, the antenna extends its -10 dB measured bandwidth from 4.57 to 6.80 GHz, catering to both 4G and 5G communication standards. Comparative analysis with an antenna lacking AMC reveals a reduced size of 34%, alongside a notable gain of 8 dBi and unidirectional radiation patterns. Additionally, a low-profile wideband two-element array, coupled with a 3×4 AMC reflector, demonstrates a broad bandwidth spanning from 4.55 to 6.8 GHz within the C-band. This configuration results in increased gains for the two antenna elements and ensures acceptable isolation exceeding 30 dB, crucial for multiple-input multiple-output (MIMO) systems. The efficiency and gain of all elements are obtained, almost 90% and 8 dBi, respectively. Moreover, an AMC unit cell, well founded on a parasitic patch, resonates at 6.12 GHz with a bandwidth extending from 5.25 to 7.15 GHz. Furthermore, the offered equivalent transmission line model of the antenna with the AMC is demonstrated, yielding desirable results. This model accurately predicts the input impedance of the 1×2 array with AMC across a broad frequency band ranging from 4.63 to 6.73 GHz. This comprehensive coverage demonstrates the effectiveness and versatility of the offered model in characterizing the electrical behavior of the antenna system across a wide frequency band, thus facilitating its design and optimization for various applications.

1. INTRODUCTION

In recent studies, electromagnetic band gap structures have found application across various wireless networks and high-frequency devices [1–4]. AMC structures, employing periodic boundary conditions across the operating band, have been adopted for cost-effective patch antennas, low-profile antennas, and mode suppression [5–10]. In a recent work [9], a broadband patch array featuring EBG-AMCs was introduced to enhance the wireless transmission rate for 5G communication. The periodic AMC surfaces without vias have been explored in [11–18]. In [16], an EBG mushroom reflector with a two-layer configuration was utilized, resulting in a 60% size reduction. However, achieving a broad AMC bandwidth remains a significant challenge [19], prompting numerous efforts [20–22]. In [22], an AMC unit cell at a resonance of 6.2 GHz with a bandwidth of 4.4% was reported, exhibiting acceptable angular stability.

The MIMO method has emerged as a crucial technology in recent wireless systems due to its ability to transmit high data rates with minimal latency [23, 24]. Achieving high port isolation has been a focus of various methods [25–28]. Several studies have proposed MIMO antennas utilizing orthogonal modes, mirrored elements, and propagation modes.

Numerous techniques have been proposed to integrate broad AMC surfaces with microstrip antennas [29, 30]. For instance, a low-profile circular polarized microstrip antenna incorporating AMC was presented in [30] to boost gain and bandwidth. Additionally, the development of two-layer boards has been prevalent in achieving improved radiation properties in most literature. The electromagnetic properties and applications of AMCs have led to a diverse range of studies aimed at enhancing antenna performance and miniaturization [31–35].

This study specifically concentrates on a proposed 2-element antenna array utilizing AMC for MIMO applications. Initially, a low-profile wideband microstrip antenna configured with two printed dipoles fed by a T-shaped feedline is designed to enlarge the impedance bandwidth. Subsequently, a parasitic AMC is demonstrated to intensify at 6.12 GHz (5.25–7.15 GHz). The printed antenna with a 3×3 parasitic AMC reflector exhibits a measured -10 dB bandwidth of 4.57–6.80 GHz, suitable for 5G and MIMO applications. Furthermore, a periodic AMC surface is integrated into the antenna by arranging a two-element array to enhance radiation properties for MIMO systems. In this regard, the printed antenna with various polarized orientations is presented, achieving an isolation of more than 30 dB between the elements for the 1×2 MIMO array.

2. PRINTED MICROSTRIP ANTENNAS WITH BROADBAND AMC

Figure 1 illustrates the overall schematic of the printed antenna, which consists of two elements featuring folded dipoles mounted on a Taconic TLT substrate ($98.4\,\text{mm} \times 98.4\,\text{mm}$, with

* Corresponding author: Hossein Malekpoor (h-malekpoor@araku.ac.ir).

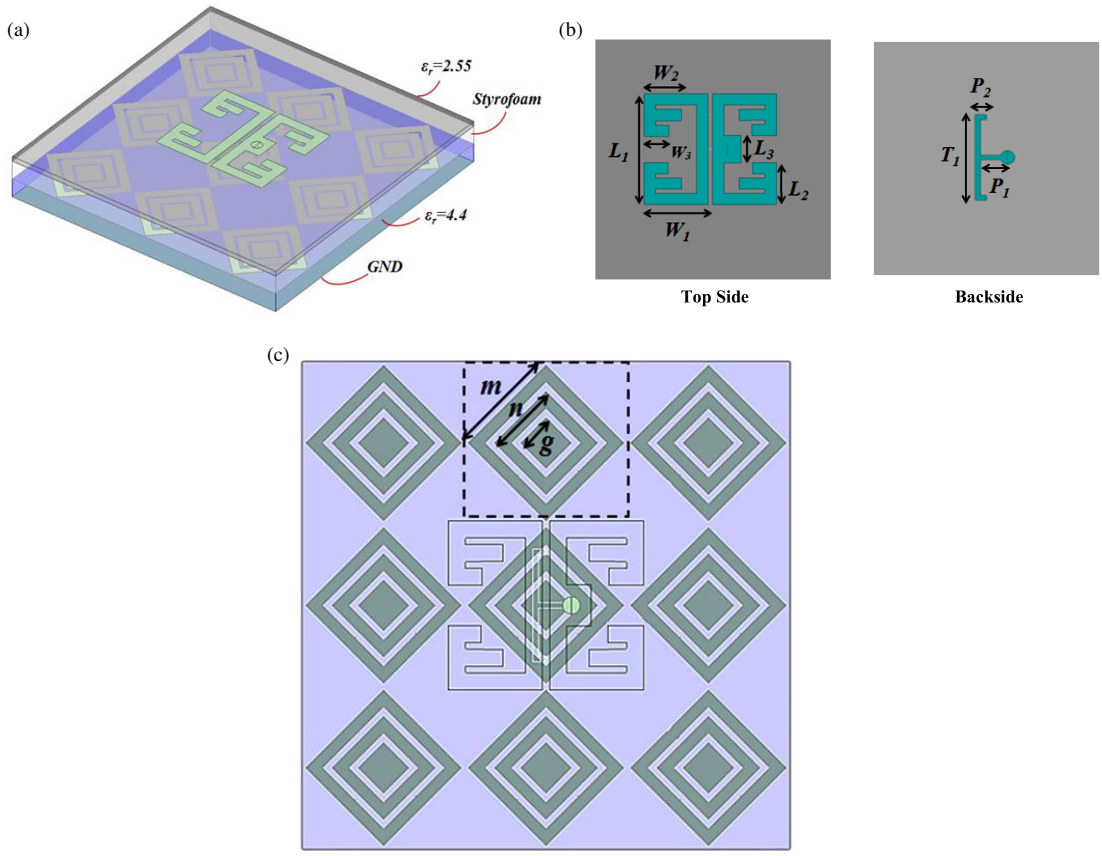

FIGURE 1. Structure of the suggested antenna by AMC reflector. (a) 3D view. (b) Top view. (c) One-element.

TABLE 1. Sizes of suggested structure.

Parameters	Values (mm)
L_1	16
L_2	3.8
L_3	4
W_1	8.9
W_2	5.2
W_3	2.6
T_1	10.6
P_1	3.13
P_2	2.1
h_1	0.8
h_2	3
h_3	3
m	3
n	6
k	0.4
l	1.1
p	1.5
L	8.2

a thickness of $h_1 = 0.8$ mm, dielectric constant of $\varepsilon_r = 2.55$, and loss tangent of 0.0006). Positioned beneath the antenna is a periodic parasitic AMC surface, separated by an air gap (Styrofoam layer) from the antenna to facilitate broadband operation. The optimal air gap distance, denoted as h_2, is determined to be 3 mm. The antenna comprises two microstrip dipoles with bent configurations on the upper layout and a T-shaped feedline on the lower layout. Each section of the antenna measures 16 mm $\times$ 8.9 mm in width and length, respectively, mounted on the substrate with dimensions of 24.6 mm $\times$ 24.6 mm. The radiating elements are excited by a coaxial feed. The specifications of the introduced design are provided in Table 1.

Figure 2 draws the schematic of a proposed unit cell for the AMC. This unit cell is constructed using an FR4 substrate with a relative permittivity (ε_r) of 4.4 and a thickness (h) of 3 mm. It is optimized with a ground plane measuring 8.2 mm $\times$ 8.2 mm. The mushroom-type electromagnetic band gap (EBG) surface is modeled using an LC resonator, whose calculation can be expressed as outlined in [11]:

$$C = \frac{W_{ebg}\varepsilon_0(1+\varepsilon_r)}{\pi}\cosh^{-1}\left(\frac{2W_{ebg}+g}{g}\right) \quad (1)$$

$$L = \mu_0 h \quad (2)$$

$$BW = \frac{1}{\eta}\sqrt{\frac{L}{C}} \quad (3)$$

The offered equivalent transmission line model for the printed array with an AMC structure aims to capture the

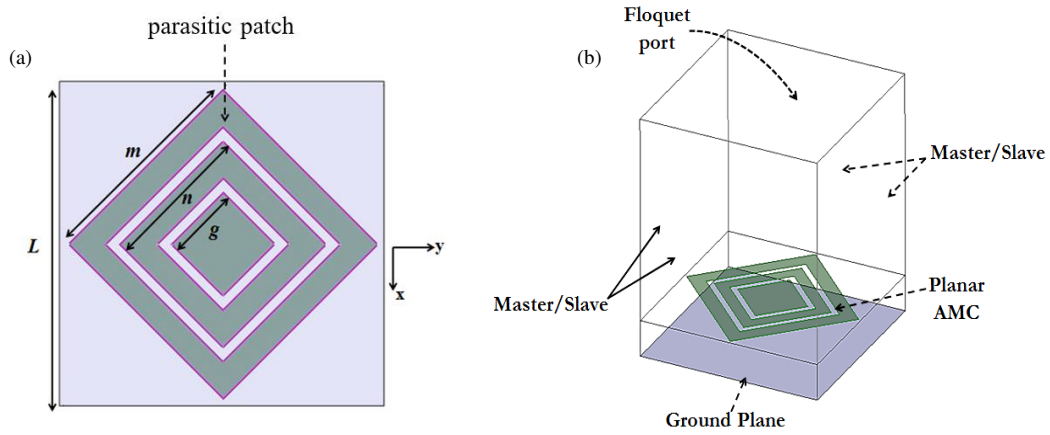

FIGURE 2. (a) AMC design and (b) periodic boundary in HFSS.

electrical characteristics of the antenna system. This model typically consists of lumped elements and transmission line segments to represent various components and their interactions. Here is an outline of the key components in the proposed model [20]:

$$C_1 = \frac{\varepsilon_e \varepsilon_0 L_e W}{2h} \cos^{-2}\left(\frac{\pi y_0}{L}\right) \tag{4}$$

$$L_1 = \frac{1}{(2\pi f_r)^2 C_1} \tag{5}$$

$$R_1 = \frac{Q}{\omega C_1} \tag{6}$$

$$Q = \frac{c\sqrt{\varepsilon_e}}{4 f_r h} \tag{7}$$

$$C_c = \frac{-(C_1+C_2)+\sqrt{((C_1+C_2)^2-4C_1C_2(1-1/C_p^2))}}{2} \tag{8}$$

$$C_p = \frac{1}{\sqrt{Q_1 Q_2}} \tag{9}$$

$$C_2 = C_1 \Delta C/(C_1 + \Delta C) \tag{10}$$

The proposed model in Figure 3 incorporates various parameters to accurately represent the behavior of the printed array with the AMC. Here are the key components and their significance. This model for the proposed printed antenna (PDA) involves two RLC resonators because of the symmetric patches. The two symmetric folded strips are represented as L_1C_1 and L_2C_2 elements according to Figure 3. Additionally, the air gap height between the antenna and AMC is modeled by the transmission line M_2. Furthermore, an LC resonator is regarded for the periodic surface.

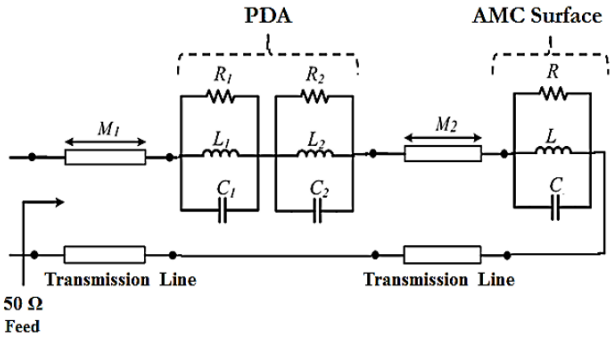

FIGURE 3. Proposed equivalent transmission line model.

The element values of the model are determined using the Agilent Advanced Design System (ADS) simulator, employing the method of moments (MOM). The optimized values of the lumped elements which are applied in the model are as follows: $R_1 = 50\,\Omega$, $C_1 = 2.58\,\text{pF}$, $L_1 = 0.251\,\text{nH}$, $R_2 = 50\,\Omega$, $C_2 = 2.73\,\text{pF}$, $L_1 = 0.267\,\text{nH}$, $R = 71\,\Omega$, $C = 0.54\,\text{pF}$, $L = 0.03\,\text{nH}$, $M_1 = 313\,\text{mm}$ and $M_2 = 3.8\,\text{mm}$.

3. EXPERIMENTAL AND SIMULATION RESULTS

Figure 4 shows the reflection magnitude and phase characteristics of the proposed artificial magnetic conductor (AMC) at an incident angle (θ) of 0°. The simulated results exhibit a ±90° reflection phase within the frequency range of 5.25–7.15 GHz, with a resonance occurring at 6.12 GHz.

Compared to previous research [11, 20–22], the suggested AMC exhibits highly acceptable characteristics. It features a symmetric unit cell design that provides identical responses for both TE and TM waves. Additionally, it offers a significantly broader bandwidth of approximately 2 GHz, maintaining acceptable stability over the AMC bandwidth. These features make it well suited for broadband applications in the C-band.

Figure 5 illustrates the S-parameters of the antenna design with and without the AMC. The antenna lacking AMC exhibits a measurement band from 5.35 to 6.7 GHz (22.4%) for $S_{11} < -10\,\text{dB}$. Conversely, the antenna equipped with the AMC demonstrates a $-10\,\text{dB}$ measured bandwidth spanning from 4.57 to 6.8 GHz, representing a bandwidth improvement of more than double.

The dimensions of the antenna without the AMC are as follows: width × length × height = $0.439\lambda_L$, $0.439\lambda_L$, and $0.014\lambda_L$, respectively. In comparison, the dimensions of the

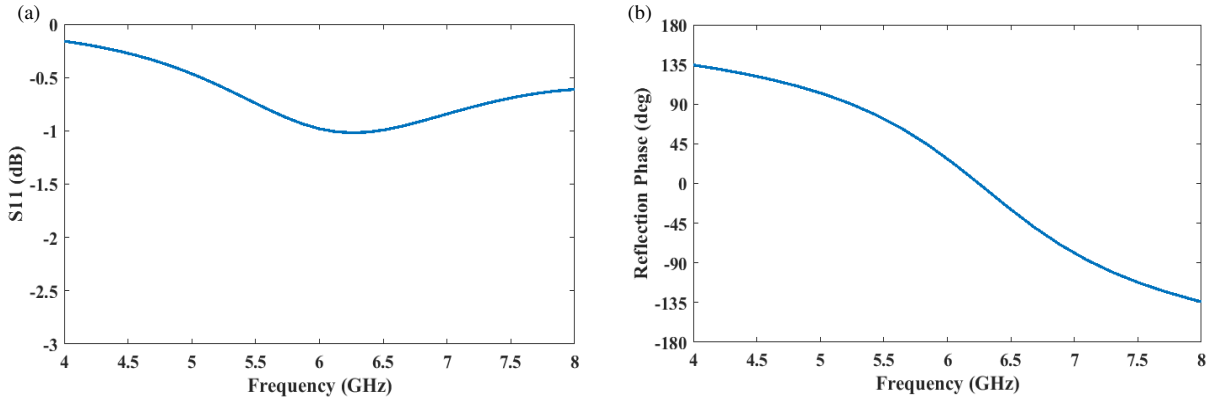

FIGURE 4. Reflection magnitude and phase of AMC for normal incident waves.

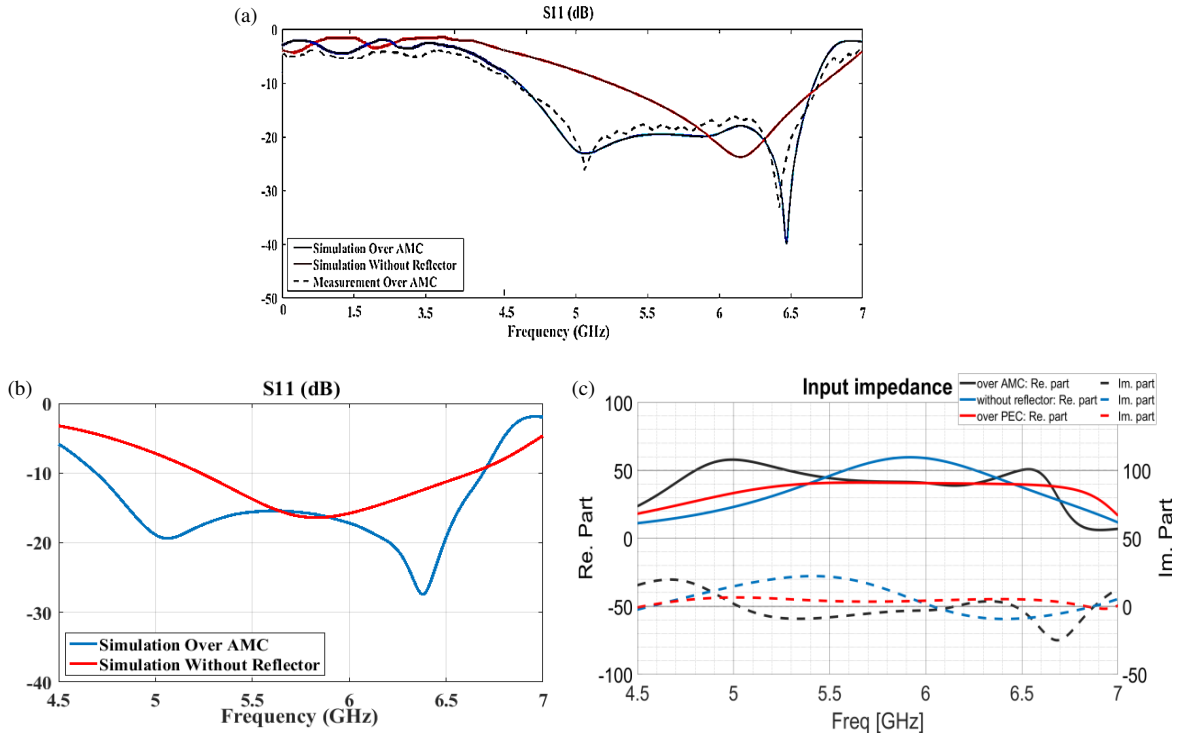

FIGURE 5. Obtained results of S-parameters. (a) HFSS, (b) proposed model, (c) input impedance.

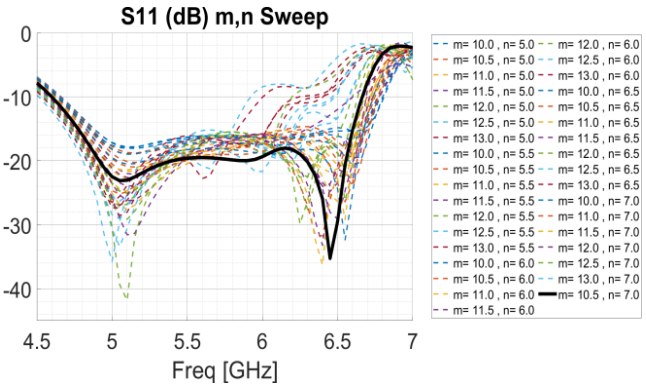

FIGURE 6. S-parameters for different lengths of the m and n parameters.

antenna with the AMC are $0.368\lambda_L$, $0.368\lambda_L$, and $0.101\lambda_L$, respectively, leading to a size reduction of 34%.

Figure 5(b) illustrates the results of the proposed equivalent model, implemented using ADS software. The simulation results cover 4.63–6.73 GHz, showcasing a good agreement with the measured results. This indicates that the equivalent model accurately captures the electrical behavior of the printed array with the AMC, providing valuable insights for the design and optimization of the antenna system.

Simulated S-parameters of the antenna with AMC for various lengths of the parameters m and n are depicted in Figure 6. Figure 7 illustrates the variations in the height of the air gap, h_2, between the antenna and the AMC. The maximum gain of the proposed antenna with the parasitic AMC across the bandwidth reaches 8 dBi, as observed in Figure 8.

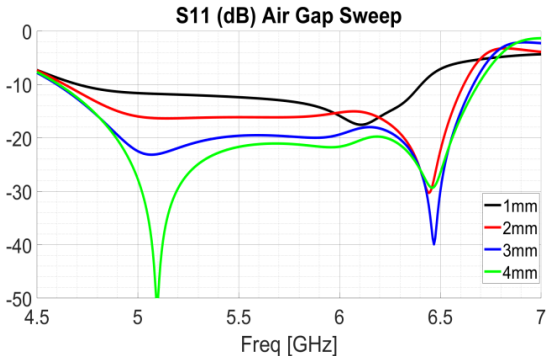

FIGURE 7. Simulated S-parameters for different h_2.

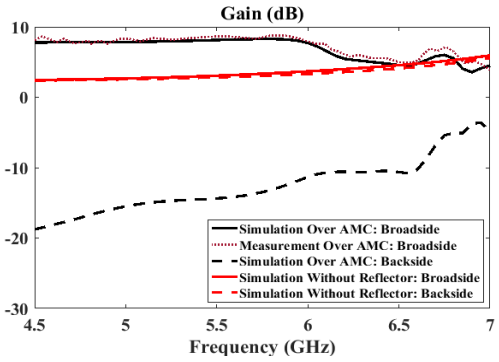

FIGURE 8. Gains of the design.

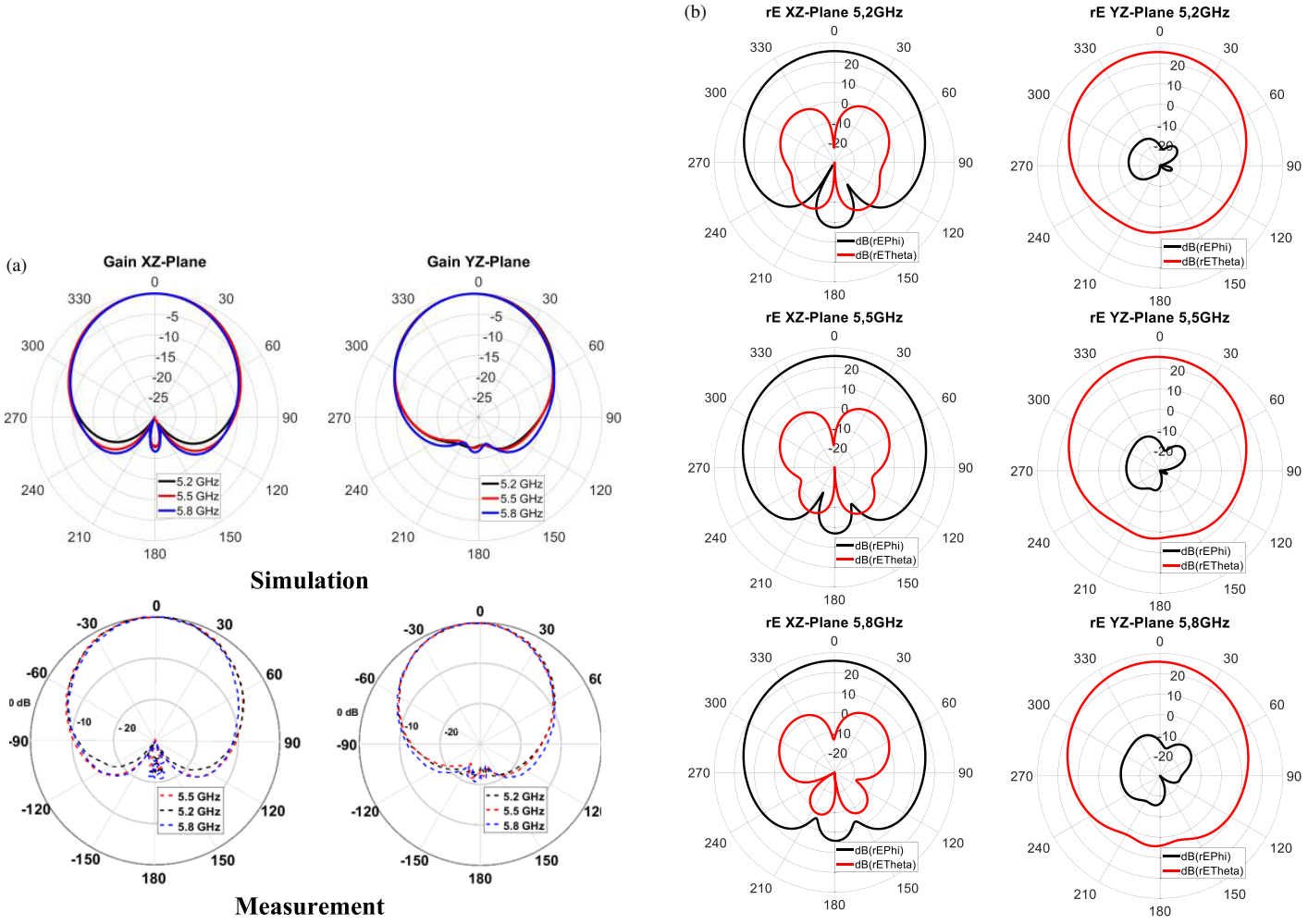

FIGURE 9. Radiation patterns for (a) gain in XZ and YZ-planes, (b) co and cross-pol in XZ and YZ-planes.

Figure 9 displays the radiation patterns in the XZ-plane and YZ-plane for the antenna design. Additionally, Figure 10 illustrates the current density distribution on the microstrip antenna and artificial magnetic conductor (AMC) at various resonances. At the lower resonance frequency of 5.1 GHz, the current distribution concentrates on the feed point, as depicted in Figure 10(a). Conversely, at the higher resonance frequency of 6.4 GHz, the current focuses on the longer section of the microstrip antenna, as shown in Figure 10(b). Table 2 lists the performance of the design with respect to its prominent properties.

4. TWO-ELEMENT MIMO ARRAY

Figure 11 depicts a two-element array designed for MIMO applications. The array features a 3×4 parasitic AMC surface measuring $24.6\,\text{mm} \times 57.4\,\text{mm}$. The distance between two printed dipoles is set to $d = 15.8\,\text{mm}$. The measured and sim-

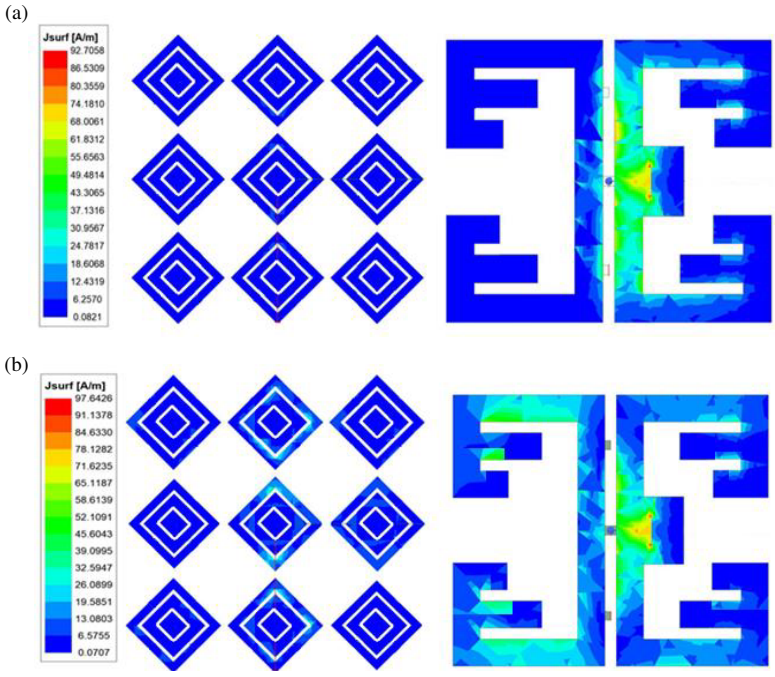

FIGURE 10. Surface current density on the patch at (a) 5.1 and (b) 6.4 GHz.

TABLE 2. Comparison study.

Proposed design	Impedance bandwidth $S_{11} \leq -10$ dB	Width × Length × Height	Maximum Gain and Efficiency
My work	4.57–6.80 GHz (46.2%)	$24.6 \times 24.6 \times 6.8\,\text{mm}^3$ $0.368\lambda_L \times 0.368\lambda_L \times 0.10\lambda_L$	8 dBi 90%
[19]	3–4.1 GHz (31%)	$75 \times 75 \times 12.7\,\text{mm}^3$ $0.75\lambda_L \times 0.75\lambda_L \times 0.127\lambda_L$	7.1 dBi 88%
[20]	3.3–3.42 GHz (3.6%) 5.88–6.1 GHz (3.7%)	$64 \times 64 \times 1.6\,\text{mm}^3$ $0.71\lambda_L \times 0.71\lambda_L \times 0.017\lambda_L$	6.29 dBi 86%
[24]	3.33–3.67 GHz (9.7%)	$70 \times 140 \times 0.8\,\text{mm}^3$ $0.77\lambda_L \times 1.55\lambda_L \times 0.009\lambda_L$	6 dBi 78%
[29]	2.37–2.50 GHz (5.34%)	$100 \times 125 \times 7.5\,\text{mm}^3$ $1.02\lambda_L \times 0.82\lambda_L \times 0.63\lambda_L$	10.3 dBi 88%
[33]	1.64–1.94 GHz (16.8%)	$50 \times 70 \times 25\,\text{mm}^3$ $0.27\lambda_L \times 0.38\lambda_L \times 0.137\lambda_L$	6.5 dBi 85%
[34]	6.9–7.9 GHz (13.5%)	$76 \times 76 \times 7\,\text{mm}^3$ $1.75\lambda_L \times 1.75\lambda_L \times 0.160\lambda_L$	13 dBi 90%
[35]	2.2–2.72 GHz (18%)	$67.5 \times 67.5 \times 4.5\,\text{mm}^3$ $0.5\lambda_L \times 0.5\lambda_L \times 0.032\lambda_L$	5 dBi 87%

ulated S-parameters of the 1×2 array with the AMC are presented in Figure 12. Specifically, the measured range of S_{11} for element 1 spans from 4.51 to 6.95 GHz, while the measured S_{22} for element 2 covers 4.60 to 6.93 GHz. Moreover, the measured S_{12} parameter indicates isolation exceeding 30 dB across the operational band, reaching a maximum of 43 dB.

Figure 13 presents three configurations of the antenna in orthogonal and horizontal orientations with the artificial magnetic conductor (AMC). These configurations are denoted as cases (a), (b), and (c). Additionally, Figure 14 plots the simulated S_{21} of the proposed designs with distinct polarized orientations. For cases (a), (b), and (c), the isolations are measured at 30 dB, 20 dB, and 19.5 dB, respectively.

In Figure 15(a), the measured gains of the two elements (1 and 2) for the proposed structure are demonstrated. Meanwhile, Figure 15(b) illustrates the measured efficiencies of the MIMO design, showing nearly identical behavior for both elements.

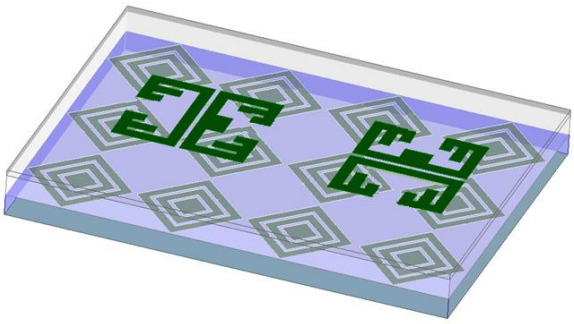

FIGURE 11. Geometry of the 1×2 array with 3×4 AMC.

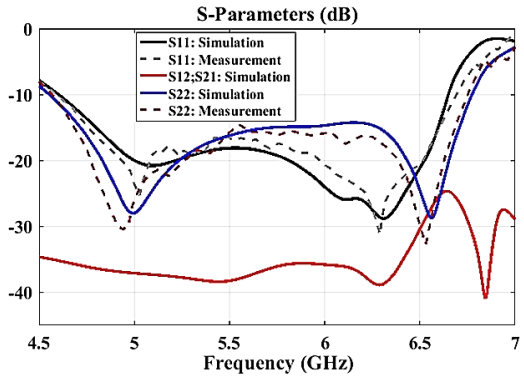

FIGURE 12. S-parameters of the 1×2 array.

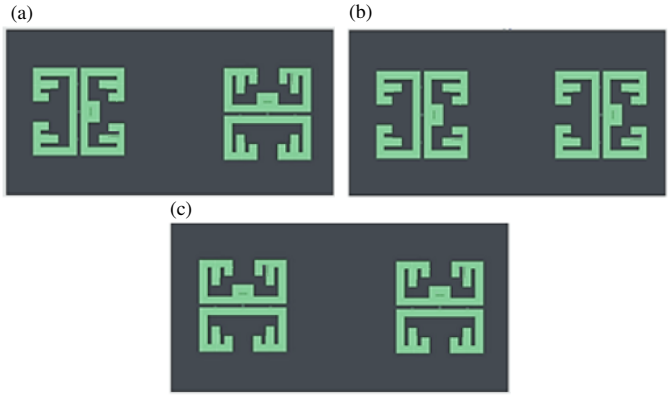

FIGURE 13. Various cases of antenna; (a) horizontal and orthogonal polarized orientations, (b) horizontal polarized orientations and (c) orthogonal polarized orientations.

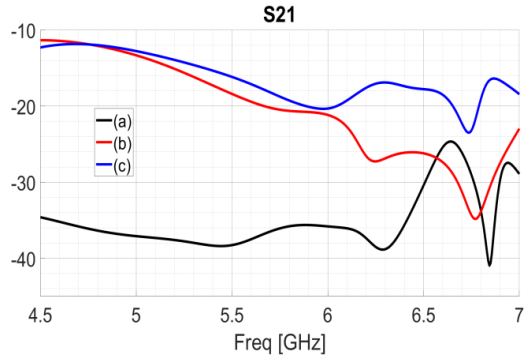

FIGURE 14. Isolations (S_{21}) of the designs in Fig. 11.

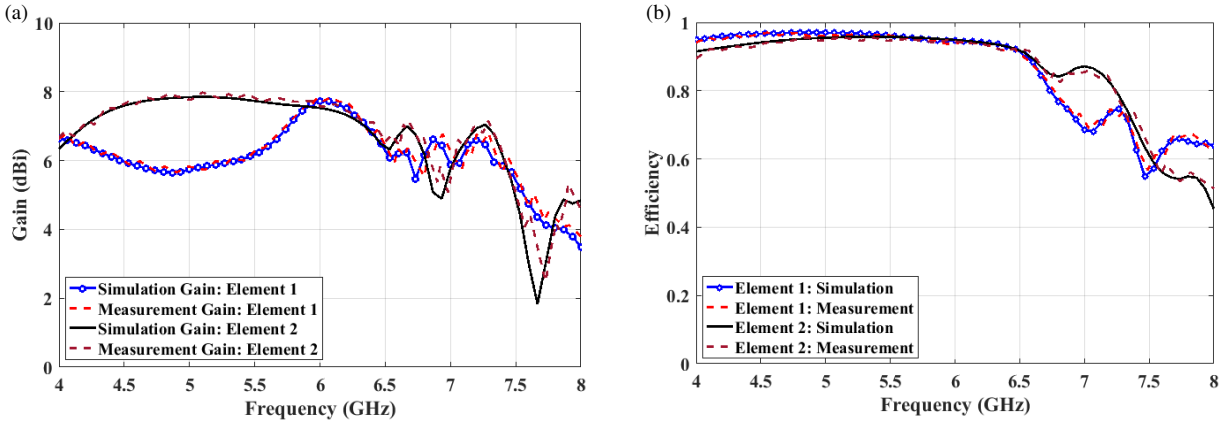

FIGURE 15. (a) Gains, (b) efficiencies of MIMO array.

Figure 16 depicts the calculated envelope correlation coefficient (ECC). The ECC level is observed to be less than 0.01 due to the proper isolation between the elements and high efficiencies. Furthermore, the measured ECC based on the S-parameters and efficiencies is provided in Figure 12. The measured ECC is calculated using the formula outlined in [36]:

$$\rho_{eij} = \frac{\left|S_{ii}^{*}S_{ij} + S_{ji}^{*}S_{jj}\right|^{2}}{\left(1-|S_{ii}|^{2}-|S_{ji}|^{2}\right)\left(1-|S_{jj}|^{2}-|S_{ij}|^{2}\right)\eta_{radi}\eta_{radj}} \quad (11)$$

The total active reflection coefficient (TARC) is defined as [37]:

$$\Gamma_{a}^{t} = \sqrt{\sum_{i=1}^{N}|b_i|^{2}} \Big/ \sqrt{\sum_{i=1}^{N}|a_i|^{2}} \quad (12)$$

where a_i is the incident wave, and b_i is the reflected wave.

The measurement of TARC for 1×2 array is sketched in Figure 17.

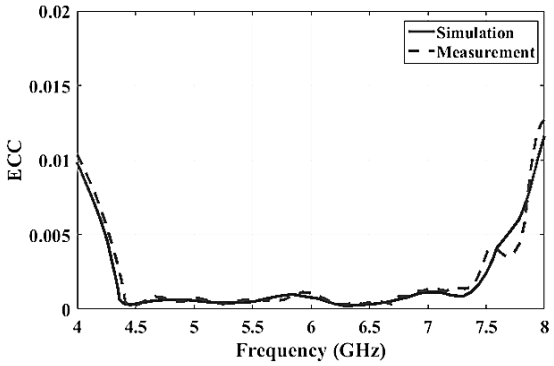

FIGURE 16. Calculated ECC 1 × 2 array.

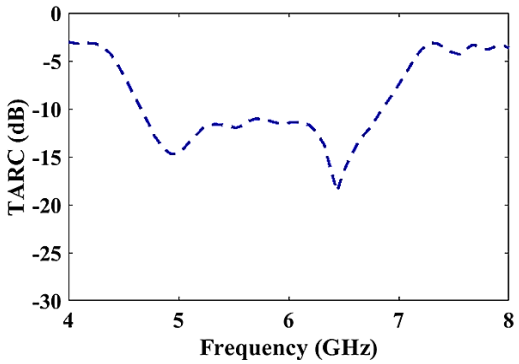

FIGURE 17. Measured TARC.

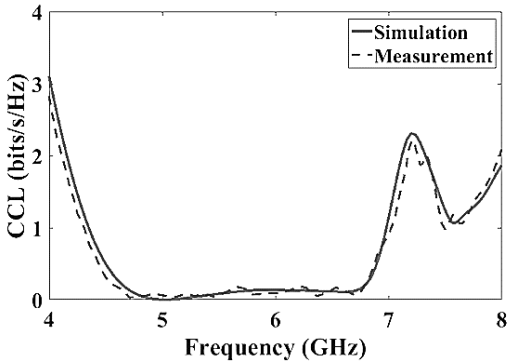

FIGURE 18. The channel capacity loss for 1 × 2 array.

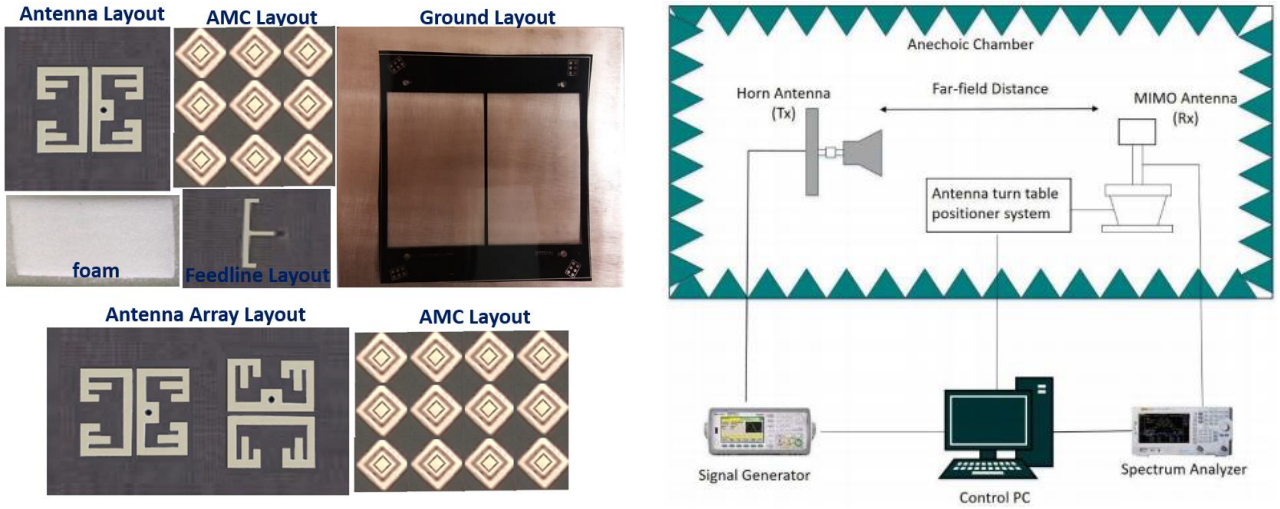

FIGURE 19. Images of fabricated cases.

In the scenario of high signal-to-noise ratio, the capacity loss is accounted for as follows:

$$\mathrm{CCL} = -\log_2 \det(\psi^R) \tag{13}$$

where ψ^R represents the receiving antenna correlation matrix [37]:

$$\psi^R = \begin{pmatrix} \rho_{1,1} & \cdots & \rho_{1,N} \\ \cdots & \cdots & \cdots \\ \rho_{N,1} & \cdots & \rho_{N,N} \end{pmatrix} \tag{14}$$

which:

$$\rho_{ii} = 1 - \left(|S_{ii}|^2 + |S_{ij}|^2\right) \tag{15}$$

$$\rho_{ij} = -\left(S_{ii}^* S_{ij} + S_{ji}^* S_{jj}\right) \tag{16}$$

The calculated capacity loss (CCL) for the 2-element MIMO array is depicted in Figure 18. Additionally, Figure 19 presents photos of the manufactured antennas.

The proposed antennas are fed by a 50-Ohm probe, and they consist of two layers with four supporter pins as air gap. The far-field performance monitoring measurement setup for assessing the radiation performance of the proposed antennas in the anechoic chamber is depicted in Figure 19. A well-calibrated standard gain horn antenna serves as the transmitting (TX) antenna, while the prototype antenna is measured as the receiving (RX) antenna. The horn antenna is positioned at a far-field distance from the proposed antenna, where D represents the total dimension of the antenna, and λ is the wavelength.

To ensure stable power reception, amplifiers are employed. During testing, the antenna is rotated to measure the radiation intensity at various orientations. The S-parameters are measured using an Agilent 8720C network analyzer. To determine the gain of the proposed antenna in dBi, the gain of the reference horn antenna (G_{ref}) is first measured. Subsequently, the gain of the proposed antenna relative to the reference antenna (G_{Relative}) is measured. The final gain of the proposed antenna is then calculated as the sum of G_{ref} and G_{Relative} for each frequency point.

5. CONCLUSION

The introduced artificial magnetic conductor (AMC) design, exhibiting broadband properties within the C-band, employs a parasitic patch to cover the frequency range of 5.25–7.15 GHz. The proposed antenna, featuring folded strips using by the AMC reflector, presents a low-profile broadband solution for wireless systems. By integrating a 3×3 AMC surface into the antenna, an impressive -10 dB impedance bandwidth of 4.57–6.80 GHz (43.2%) is achieved, accompanied by unidirectional radiation patterns and higher gains up to 8 dBi. Measurement results confirm acceptable efficiency, leading to the conclusion that the suggested design is suitable for broadband wireless systems. Moreover, the performance of a two-element array of the antenna is investigated using a 3×4 AMC reflector. In summary, the realized study underscores the potential of the compact MIMO antenna array, boasting high gains of 8 dBi and efficiencies, for applications in WLAN, WiMAX, and 5G systems. Overall, the proposed equivalent transmission line model aims to provide a simplified yet accurate representation of the printed array with the AMC, allowing for efficient analysis and design optimization of the antenna system.

REFERENCES

[1] Malekpoor, H. and S. Jam, "Design, analysis, and modeling of miniaturized multi-band patch arrays using mushroom-type electromagnetic band gap structures," *International Journal of RF and Microwave Computer-Aided Engineering*, Vol. 28, No. 6, e21 404.1–13, 2018.

[2] Yang, X., Y. Liu, Y.-X. Xu, and S.-X. Gong, "Isolation enhancement in patch antenna array with fractal UC-EBG structure and cross slot," *IEEE Antennas and Wireless Propagation Letters*, Vol. 16, 2175–2178, 2017.

[3] Jam, S. and H. Malekpoor, "Compact 1×4 patch antenna array by means of EBG structures with enhanced bandwidth," *Microwave and Optical Technology Letters*, Vol. 58, No. 12, 2983–2989, 2016.

[4] Althuwayb, A. A., "Enhanced radiation gain and efficiency of a metamaterial-inspired wideband microstrip antenna using substrate integrated waveguide technology for sub-6 GHz wireless communication systems," *Microwave and Optical Technology Letters*, Vol. 63, No. 7, 1892–1898, Jul. 2021.

[5] Foroozesh, A. and L. Shafai, "Effects of artificial magnetic conductors in the design of low-profile high-gain planar antennas with high-permittivity dielectric superstrate," *IEEE Antennas and Wireless Propagation Letters*, Vol. 8, 10–13, 2008.

[6] Alibakhshikenari, M., F. Babaeian, B. S. Virdee, S. Aïssa, L. Azpilicueta, C. H. See, A. A. Althuwayb, I. Huynen, R. A. Abd-Alhameed, F. Falcone, and E. Limiti, "A comprehensive survey on 'Various decoupling mechanisms with focus on metamaterial and metasurface principles applicable to SAR and MIMO antenna systems'," *IEEE Access*, Vol. 8, 192 965–193 004, 2020.

[7] Malekpoor, H., "Comparative investigation of reflection and band gap properties of finite periodic wideband artificial magnetic conductor surfaces for microwave circuits applications in X-band," *International Journal of RF and Microwave Computer-Aided Engineering*, Vol. 29, No. 10, e21 874.1–13, 2019.

[8] Bell, J. M., M. F. Iskander, and J. J. Lee, "Ultrawideband hybrid EBG/ferrite ground plane for low-profile array antennas," *IEEE Transactions on Antennas and Propagation*, Vol. 55, No. 1, 4–12, 2007.

[9] Nashaat, D., H. A. Elsadek, E. A. Abdallah, M. F. Iskander, and H. M. Elhenawy, "Ultrawide bandwidth 2×2 microstrip patch array antenna using electromagnetic band-gap structure (EBG)," *IEEE Transactions on Antennas and Propagation*, Vol. 59, No. 5, 1528–1534, 2011.

[10] Barth, S. and A. K. Iyer, "A miniaturized uniplanar metamaterial-based EBG for parallel-plate mode suppression," *IEEE Transactions on Microwave Theory and Techniques*, Vol. 64, No. 4, 1176–1185, 2016.

[11] Sievenpiper, D., L. Zhang, R. F. J. Broas, N. G. Alexopolous, and E. Yablonovitch, "High-impedance electromagnetic surfaces with a forbidden frequency band," *IEEE Transactions on Microwave Theory and Techniques*, Vol. 47, No. 11, 2059–2074, 1999.

[12] Deng, J., J. Li, L. Zhao, and L. Guo, "A dual-band inverted-F MIMO antenna with enhanced isolation for WLAN applications," *IEEE Antennas and Wireless Propagation Letters*, Vol. 16, 2270–2273, 2017.

[13] Rajagopal, S., G. Chennakesavan, D. R. P. Subburaj, R. Srinivasan, and A. Varadhan, "A dual polarized antenna on a novel broadband multilayer Artificial Magnetic Conductor backed surface for LTE/CDMA/GSM base station applications," *AEU — International Journal of Electronics and Communications*, Vol. 80, 73–79, 2017.

[14] Lee, H. and B. Lee, "Compact broadband dual-polarized antenna for indoor MIMO wireless communication systems," *IEEE Transactions on Antennas and Propagation*, Vol. 64, No. 2, 766–770, 2016.

[15] Ameri, E., S. H. Esmaeli, and S. H. Sedighy, "Wide band radar cross section reduction by thin AMC structure," *AEU — International Journal of Electronics and Communications*, Vol. 93, 150–153, 2018.

[16] Ghosh, S., T.-N. Tran, and T. Le-Ngoc, "Dual-layer EBG-based miniaturized multi-element antenna for MIMO systems," *IEEE Transactions on Antennas and Propagation*, Vol. 62, No. 8, 3985–3997, 2014.

[17] Liu, X., Y. Di, H. Liu, Z. Wu, and M. M. Tentzeris, "A planar Windmill-like broadband antenna equipped with artificial mag-

netic conductor for off-body communications," *IEEE Antennas and Wireless Propagation Letters*, Vol. 15, 64–67, 2015.

[18] Yang, S., Y. Chen, C. Yu, Y. Gong, and F. Tong, "Design of a low-profile, frequency-reconfigurable, and high gain antenna using a varactor-loaded AMC ground," *IEEE Access*, Vol. 8, 158 635–158 646, 2020.

[19] Zhu, J., S. Li, S. Liao, and Q. Xue, "Wideband low-profile highly isolated MIMO antenna with artificial magnetic conductor," *IEEE Antennas and Wireless Propagation Letters*, Vol. 17, No. 3, 458–462, 2018.

[20] Ghosh, A., V. Kumar, G. Sen, and S. Das, "Gain enhancement of triple-band patch antenna by using triple-band artificial magnetic conductor," *IET Microwaves, Antennas & Propagation*, Vol. 12, No. 8, 1400–1406, 2018.

[21] Othman, N., N. A. Samsuri, M. K. A. Rahim, and K. Kamardin, "Low specific absorption rate and gain-enhanced meandered bowtie antenna utilizing flexible dipole-like artificial magnetic conductor for medical application at 2.4 GHz," *Microwave and Optical Technology Letters*, Vol. 62, No. 12, 3881–3889, 2020.

[22] Hadarig, R. C., M. E. De Cos, and F. Las-Heras, "Novel miniaturized artificial magnetic conductor," *IEEE Antennas and Wireless Propagation Letters*, Vol. 12, 174–177, 2013.

[23] De Sena, A. S., D. B. D. Costa, Z. Ding, and P. H. J. Nardelli, "Massive MIMO-NOMA networks with multi-polarized antennas," *IEEE Transactions on Wireless Communications*, Vol. 18, No. 12, 5630–5642, 2019.

[24] Xu, Z. and C. Deng, "High-isolated MIMO antenna design based on pattern diversity for 5G mobile terminals," *IEEE Antennas and Wireless Propagation Letters*, Vol. 19, No. 3, 467–471, 2020.

[25] Wang, Z., G. Zhang, Y. Yin, and J. Wu, "Design of a dual-band high-gain antenna array for WLAN and WiMAX base station," *IEEE Antennas and Wireless Propagation Letters*, Vol. 13, 1721–1724, 2014.

[26] Jam, S. and H. Malekpoor, "Analysis on wideband patch arrays using unequal arms with equivalent circuit model in X-band," *IEEE Antennas and Wireless Propagation Letters*, Vol. 15, 1861–1864, 2016.

[27] Malekpoor, H. and M. Hamidkhani, "Bandwidth and gain improvement for reduced size of stacked microstrip antenna fed by folded triangular patch with half V-shaped slot," *International Journal of RF and Microwave Computer-Aided Engineering*, Vol. 31, No. 6, e22649, 2021.

[28] Hamidkhani, M., H. Malekpoor, and H. Oraizi, "Oscillator phase-noise reduction using high-QSC active Giuseppe Peano fractal resonators," *IEEE Microwave and Wireless Components Letters*, Vol. 29, No. 5, 354–356, 2019.

[29] Joubert, J., J. C. Vardaxoglou, W. G. Whittow, and J. W. Odendaal, "CPW-fed cavity-backed slot radiator loaded with an AMC reflector," *IEEE Transactions on Antennas and Propagation*, Vol. 60, No. 2, 735–742, 2012.

[30] Feng, D., H. Zhai, L. Xi, S. Yang, K. Zhang, and D. Yang, "A broadband low-profile circular-polarized antenna on an AMC reflector," *IEEE Antennas and Wireless Propagation Letters*, Vol. 16, 2840–2843, 2017.

[31] Malekpoor, H. and S. Jam, "Improved radiation performance of low profile printed slot antenna using wideband planar AMC surface," *IEEE Transactions on Antennas and Propagation*, Vol. 64, No. 11, 4626–4638, 2016.

[32] Liu, J., J.-Y. Li, J.-J. Yang, Y.-X. Qi, and R. Xu, "AMC-loaded low-profile circularly polarized reconfigurable antenna array," *IEEE Antennas and Wireless Propagation Letters*, Vol. 19, No. 7, 1276–1280, 2020.

[33] Zhong, Y.-W., G.-M. Yang, and L.-R. Zhong, "Gain enhancement of bow-tie antenna using fractal wideband artificial magnetic conductor ground," *Electronics Letters*, Vol. 51, No. 4, 315–317, 2015.

[34] Turpin, J. P., Q. Wu, D. H. Werner, B. Martin, M. Bray, and E. Lier, "Near-zero-index metamaterial lens combined with AMC metasurface for high-directivity low-profile antennas," *IEEE Transactions on Antennas and Propagation*, Vol. 62, No. 4, 1928–1936, 2014.

[35] Raad, H. R., A. I. Abbosh, H. M. Al-Rizzo, and D. G. Rucker, "Flexible and compact AMC based antenna for telemedicine applications," *IEEE Transactions on Antennas and Propagation*, Vol. 61, No. 2, 524–531, 2013.

[36] Vaughan, R. G. and J. B. Andersen, "Antenna diversity in mobile communications," *IEEE Transactions on Vehicular Technology*, Vol. 36, No. 4, 149–172, Nov. 1987.

[37] Chae, S. H., S.-K. Oh, and S.-O. Park, "Analysis of mutual coupling, correlations, and TARC in WiBro MIMO array antenna," *IEEE Antennas and Wireless Propagation Letters*, Vol. 6, 122–125, 2007.